Plasma environmental effects in the atomic structure for simulating x-ray free-electron-laser-heated solid-density matter

Rui Jin [1,*] Zoltan Jurek,[1,2] Robin Santra [1,2,3] and Sang-Kil Son [1,2,†]

[1]*Center for Free-Electron Laser Science CFEL, Deutsches Elektronen-Synchrotron DESY, Notkestrasse 85, 22607 Hamburg, Germany*
[2]*The Hamburg Centre for Ultrafast Imaging, Luruper Chaussee 149, 22761 Hamburg, Germany*
[3]*Department of Physics, Universität Hamburg, Notkestrasse 9-11, 22607 Hamburg, Germany*

High energy density (HED) matter exists extensively in the Universe, and it can be created with extreme conditions in laboratory facilities such as x-ray free-electron lasers (XFEL). In HED matter, the electronic structure of individual atomic ions is influenced by a dense plasma environment, and one of the most significant phenomena is the ionization potential depression (IPD). Incorporation of the IPD effects is of great importance in accurate modeling of dense plasmas. All theoretical treatments of IPD so far have been based on the assumption of local thermodynamic equilibrium, but its validity is questionable in ultrafast formation dynamics of dense plasmas, particularly when interacting with intense XFEL pulses. A treatment of transient IPD, based on an electronic-structure calculation of an atom in the presence of a plasma environment described by classical particles, has recently been proposed [Phys. Rev. E **103**, 023203 (2021)], but its application to and impact on plasma dynamics simulations have not been investigated yet. In this work, we extend XMDYN, a hybrid quantum-classical approach combining Monte Carlo and molecular dynamics, by incorporating the proposed IPD treatment into plasma dynamics simulations. We demonstrate the importance of the IPD effects in theoretical modeling of aluminum dense plasmas by comparing two XMDYN simulations: one with electronic-structure calculations of isolated atoms (without IPD) and the other with those of atoms embedded in a plasma (with IPD). At equilibrium, the mean charge obtained in the plasma simulation with IPD is in good agreement with the full quantum-mechanical average-atom model. The present approach promises to be a reliable tool to simulate the creation and nonequilibrium evolution of dense plasmas induced by ultraintense and ultrashort XFEL pulses.

I. INTRODUCTION

High energy density (HED) matter is a type of strongly coupled system of typical energy density 10^{11} J/m^3 [1]. It exists extensively in the Universe, from hot dense plasmas such as those in supernovae and stellar interiors [2,3], to warm dense plasmas such as those in planetary interiors [4–7]. HED matter is now routinely generated in laboratories such as inertial confinement fusion (ICF) [8,9] and x-ray free-electron laser (XFEL) [10,11] facilities, where the HED condition is achieved by compressing the system with high pressure or heating the system with high-intensity lasers within ultrashort time. In particular, the high brilliance and spatial coherence of the XFEL pulses make it possible to uniformly heat bulk matter and create and probe warm dense plasmas on a femtosecond timescale [12].

A theoretical treatment of HED matter is crucial to help design and understand such experiments. It is challenging because HED matter lies on the border between condensed-matter physics and plasma physics, and it is necessary to treat both thermal Coulomb coupling and quantum effects on an equal footing. In addition, the plasmas created by XFELs are considered to be far from local thermodynamic equilibrium (LTE) [13], because the electron-ion relaxation timescale of picoseconds [14,15] is much longer than typical XFEL pulse durations of femtoseconds. Nevertheless, many theoretical approaches rely on the LTE condition. In this case, it is commonly assumed that electrons are hot and ions remain cold [16], or they are modeled by the two-temperature method [17,18], where electrons and ions are assumed to separately thermalize instantaneously. Alternatively, XFEL-created plasmas can be described by non-LTE (NLTE) approaches [19–24], where detailed atomic dynamics are taken into account in the kinetic simulation based on the collisional-radiative (CR) model [25,26]. To better incorporate the nonlocality and nonthermal features of the XFEL-created dense plasmas, a hybrid quantum-classical approach based on a Monte Carlo molecular dynamics (MC-MD) scheme [27,28] has been proposed, where the atomic electronic structure is calculated quantum mechanically, and the free electrons and ions are treated as classical particles.

In dense plasmas, the atoms experience screening by the plasma environment, giving rise to a phenomenon called ionization potential depression (IPD), where the atomic energy levels are shifted and some bound states are moved to the continuum. This phenomenon is critical for correctly understanding and modeling atomic processes in dense plasmas. Historically, two analytical models based on thermal equilibrium were formulated to effectively evaluate the IPD values: the Stewart-Pyatt (SP) [29] and Ecker-Kröll (EK) [30] models.

---
*rui.jin@cfel.de
†sangkil.son@cfel.de

A recent spectroscopic experiment driven by a high-power optical laser shock [31,32] was better explained by the SP model, whereas the EK model was reported to better fit another recent experiment using an XFEL [12,33]. Thereafter, extensive IPD measurements [34–39] and theoretical calculations [40–49], as well as *ab initio* electronic structure calculations of the IPD effects [16,50–54], have been carried out to settle the debate.

All the above-mentioned IPD effects are obtained under the LTE condition, even when they are employed in NLTE simulations [19–21,26]. Moreover, CR modeling mostly utilizes detailed balancing [20,26,37] for treating collisional ionization and recombination, which relies on thermal equilibrium of the free electrons. Even though the electron plasma is treated separately, it undergoes nonequilibrium electron dynamics driven by intense XFEL pulses [55], which is anticipated by the fact that the electron-electron relaxation timescale [56–58] is comparable to the XFEL pulse duration. Furthermore, nonthermal femtosecond phase transitions induced by intense XFEL pulses have been reported [59,60]. Therefore, it is desirable to implement an IPD treatment that is unrestricted by the thermal equilibrium condition in the simulation. To address such inconsistent usage of LTE IPD in NLTE simulations, a treatment of transient IPD without assuming thermal equilibrium has recently been proposed [61] and tested in comparison with LTE IPD and available experimental data [12,33]. The proposed NLTE IPD treatment is based on an electronic-structure calculation that employs real-time information from a classical MD simulation; it is not based on an analytical IPD expression as in the SP and EK models. Implementation of the proposed IPD treatment into NLTE simulations is challenging, because it demands mutual communication between dynamics simulation and atomic-structure calculation on the fly. To the best of our knowledge, there has been no NLTE simulation of plasma dynamics incorporating NLTE IPD effects based on on-the-fly atomic-structure calculations. In the present work, we implement the plasma environmental effects including transient IPD in an MC-MD approach to simulate formation dynamics of dense plasmas.

This paper is organized as follows. In Sec. II, we provide a theoretical description of constructing the classical environmental potential in atomic-structure calculations and a consistent treatment of ionization processes in the presence of the IPD effects and the plasma environment. In Sec. III, we employ our MC-MD implementation to simulate a solid-density Al plasma driven by intense XFEL pulses. Analyzing charge-state populations, energy depositions, and individual physical processes, we compare simulations of plasma formation dynamics with and without the plasma environmental effects in atomic-structure calculations. The equilibrium state calculated using the new implementation is compared with a quantum-mechanical average-atom model as a benchmark. We conclude with a short summary and an outlook in Sec. IV.

II. METHODOLOGY

A. Monte Carlo molecular dynamics implementation

We employ a Monte Carlo molecular dynamics (MC-MD) simulation tool, XMDYN [27,28], to describe the time propagation of XFEL-driven nonequilibrium dense plasmas. In this MC-MD scheme, the bound electrons are assigned to nuclei to be described as atomic ions. The external or translational degrees of freedom of the atomic ions and free electrons are treated with a classical MD technique. The dynamics of the configuration of bound electrons in individual atomic ions, which is represented by the occupation numbers of the orbitals, are computed in a stochastic framework via an MC algorithm. The atomic electron structure is calculated on the fly using the x-ray atomic toolkit, XATOM [28,62], which is based on the Hartree-Fock-Slater (HFS) method. The photoionization cross sections and the rates of Auger-Meitner decay [63] and fluorescence are calculated quantum mechanically within XATOM for individual electron configurations of atomic ions. Furthermore, complex many-body collisional processes, i.e., collisional ionization and recombination, are implemented using semiclassical algorithms within XMDYN. At an ionization event, a quantum electron is converted into a classical one: a new classical particle (with charge and mass of an electron) is created in the vicinity of the parent ion with a kinetic energy set by energy conservation, while the occupation number of the parent orbital is decreased by 1. At recombination, the inverse procedure is executed. This hybrid XMDYN-XATOM approach has been demonstrated to reproduce electron kinetic energy spectra and ion distributions from rare-gas nanoplasmas [64–67], the fragmentation dynamics of C_{60} [27,68], the Coulomb explosion imaging of iodopyridine [69], and the dynamics of disulfide expansion in thaumatin [70]. It has been recently extended to simulate bulk systems using the supercell approach and periodic boundary conditions [61,71–73].

The transient IPD effects are considered via the recently developed XPOT code [61], where an NLTE approach is employed and atomic-structure calculations are performed, taking into account the real-space charge distribution obtained directly from MD simulation snapshots. These NLTE IPD effects, however, have not been taken into consideration in the way the MC-MD simulations are performed. In the original implementation of XMDYN, the atomic ions are treated individually as isolated entities free from a plasma environment. The atomic structure (orbitals and orbital energies) and atomic data (cross sections and rates) are obtained from the respective isolated-atom calculation. This can cause overestimation of ionization thresholds and underestimation of kinetic energies for the ionized electrons in dense plasmas. In the present work, we introduce IPD feedback into the MC-MD approach. The atomic structure and atomic data are calculated in the presence of a plasma environment, and the implications of the IPD effects are incorporated into every single dynamical process in XMDYN simulations. In the following, we employ the term XMDYN for the original version and XMDYN-IPD for the new implementation including IPD feedback from the atomic-structure calculation.

B. Atomic-structure calculation with a plasma environment

The electrons in an atom embedded in a plasma experience a complex real-space potential landscape rather than the spherically symmetric potential in an isolated atom. The muffin-tin approximation is widely used for solid-state calculations to provide reasonably accurate band structure

with comparably low computational cost [16,74]. Within this approximation, the potential in the center region is treated as being spherically symmetric, while the potential in the interstitial region is approximated by a constant potential tail V_0, due to the delocalized feature of the band electrons. Hence, the potential used in an atomic-structure calculation is given by

$$V_A^{\text{pla}}(r) = \begin{cases} V_A^{\text{atom}}(r) + V_{q=q_A}^{\text{env}}(r) & \text{for } r < r_c, \\ V_0 & \text{for } r \geqslant r_c, \end{cases} \quad (1)$$

where $V_A^{\text{atom}}(r)$ is the atomic potential treated in the Hartree-Fock-Slater (HFS) model and to be determined by a self-consistent-field (SCF) calculation with the bound-electron density for the given atom A in the presence of the additional environmental potential. In HFS, the electron density is assumed to be spherically symmetric. Note that the point r_c is determined in every single SCF iteration by matching the fixed potential tail V_0; r_c is not a fixed parameter as in conventional muffin-tin-type calculations. Here, $V_{q=q_A}^{\text{env}}(r)$ is the external environmental potential based on a snapshot of the classical particles at any given time,

$$V_A^{\text{env}}(r) = -\sum_{i \neq A} q_i \frac{\sqrt{(r+r_i)^2 + a^2} - \sqrt{(r-r_i)^2 + a^2}}{2rr_i}, \quad (2)$$

$$V_{q=q_A}^{\text{env}}(r) = \frac{1}{N_q} \sum_A^q V_A^{\text{env}}(r), \quad (3)$$

where q_i and r_i are the charge and the radial position (with respect to the position of A) of the ith classical particle, respectively, and a is a soft-core radius to avoid the Coulomb singularity [28]. Note that Eq. (2) is the result after spherical averaging of the environmental potential, and Eq. (3) corresponds to the charge-selective averaging scheme proposed in Ref. [61], where N_q indicates the number of atomic ions with the charge q.

In principle, the potential tail V_0 also needs to be computed self-consistently, taking into account all atomic ions in the entire supercell. To avoid such complexity, we approximate V_0 with a touching potential algorithm as described in Ref. [61]. The basic concept is to obtain a match of the potentials of neighboring atoms. For instance, the touching potential value for A and B separated by a distance r_{AB} is $V_{AB} = V_A^{\text{approx}}(r_T) = V_B^{\text{approx}}(r_{AB} - r_T)$, which defines the touching sphere radius r_T with respect to atom A. Originally, the approximated potential experienced by the inspected bound electron was given by $V_A^{\text{approx}}(r) = -(q_A + 1)/r + V_A^{\text{env}}(r)$, where $V_A^{\text{env}}(r)$ is the environmental potential in Eq. (2) before the charge-selective averaging scheme. In the present method, $V_A^{\text{env}}(r)$ used in the approximated potential is replaced with the charge-selective averaged potential, i.e., $V_A^{\text{approx}}(r) = -(q_A + 1)/r + V_{q=q_A}^{\text{env}}(r)$, in order to be consistent with the environmental potential used in Eq. (1). The two different choices produce similar IPD values within ~10% as shown in Fig. 8 in Appendix A. The global muffin-tin potential tail is given by the average over all atomic pairs, i.e., $V_0 = \langle V_{AB} \rangle_{\text{all pairs}}$, not by $V_0 = \min\{V_{AB}\}$ as falsely suggested in Ref. [61].

Introducing the potential tail V_0 in the atomic-structure calculation implies that electrons whose orbital energies are above V_0 become unbound. These electrons are treated as
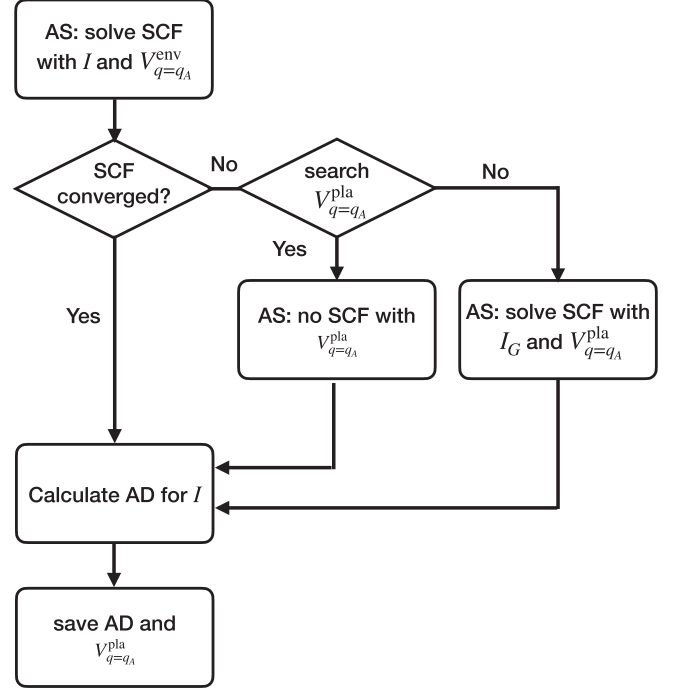

FIG. 1. Fallback strategies for atomic-structure calculations. AS denotes atomic structure, AD denotes atomic data, I is the given configuration, and I_G is the ground configuration for the given charge q_A.

being "ionized" after the respective SCF calculation (see the next section). However, if these electrons in the energy levels close to or above V_0 are part of the SCF calculation as bound electrons, which happens in excited-state calculations, they cause SCF convergence problems. Loosening r_c during SCF iterations in our scheme also hinders SCF convergence. Therefore, we introduce a set of fallback strategies in cases of SCF failure illustrated in Fig. 1. At any given snapshot in the MC-MD simulation, we try to calculate the atomic structure of A for its current electron configuration and its current environmental potential $V_{q=q_A}^{\text{env}}(r)$. If the SCF procedure succeeds, we calculate the atomic data and save them as well as the full plasma potential V^{pla} as the latest potential belonging to a given charge state q_A, denoted as $V_{q=q_A}^{\text{pla}}$. If the SCF calculation fails, we search for the latest potential belonging to the same q_A and obtain the atomic structure using the loaded potential with no SCF iterations. If the requested potential is unavailable, then we run an SCF calculation with the ground configuration for the given charge under the given environmental potential, which typically provides a converged solution. Then we calculate the atomic data for the given electron configuration. With these strategies, we were able to provide atomic structure and atomic data to the MC-MD part of our simulations without any interruption due to SCF failures.

To account for all important dynamics, the quantum atomic properties need to be updated within the characteristic timescale of significant changes in the evolution of the environmental potential $V_{q=q_A}^{\text{env}}(r)$, which is limited by the fastest atomic dynamical process. In practice, one needs to examine convergence of the simulated physical quantities

such as temperature and charge state distribution by varying the time step employed for updating the environmental potential. In the current work, we used a time step of 0.1 fs to take snapshots of the MC-MD simulation results, and numerically confirmed that it provided satisfactory results. Note that this time step is larger than $\Delta t = 0.5$ attoseconds, which is used for time propagation in XMDYN, because the environmental potential varies smoothly on the femtosecond timescale after applying the charge-selective averaging scheme.

C. Treatment of ionization processes with the potential tail

We have introduced the flat potential V_0 in the atomic-structure calculation. The energy levels below V_0 are considered bound states, whereas the energy levels above V_0 are defined as continuum states. Thus the excitation of an electron from a bound state to the continuum threshold located at V_0 defines the ionization potential in the plasma calculation,

$$\text{IP}_{I,j}^{\text{pla}} = V_0 - \varepsilon_{I,j}^{\text{pla}}, \tag{4}$$

where I and j denote the electron configuration and the orbital index, respectively, and ε^{pla} is the orbital energy calculated under the plasma environmental potential. Then, the corresponding IPD is defined as the difference between the ionization potentials of the atom in isolation and of the atom in the plasma environment,

$$\Delta E_{I,j} = \text{IP}_{I,j}^{\text{iso}} - \text{IP}_{I,j}^{\text{pla}}, \tag{5}$$

where $\text{IP}_{I,j}^{\text{iso}} = -\varepsilon_{I,j}^{\text{iso}}$ obtained from the corresponding isolated-atom calculation with the same electron configuration I.

In the previous implementation of XMDYN, the atomic-structure calculation was based on the isolated-atom calculation, thus ignoring the IPD effects and employing the classical dynamics only for electrons with a non-negative energy. By introducing the potential tail V_0, it is consistent with the hybrid framework to treat electrons below V_0 quantum mechanically and to use the classical dynamics to describe electrons above V_0. All ionization processes, including photoionization, collisional ionization, and Auger-Meitner decay, will be affected by ionization-threshold lowering (IPD). In addition, the electrons located in the energy levels above the potential tail in the atomic-structure calculation are supposed to be immediately "ionized" into continuum states. This process is implemented in the same way as other ionization processes within XMDYN, i.e., by converting a quantum bound electron into a classical unbound electron with a kinetic energy that, in this case, is given by $E_{\text{kin}} = \varepsilon_{I,j}^{\text{pla}} - V_0$. Note that this instantaneous transfer from quantum to classical electrons effectively mimics the pressure ionization [75] in the dense plasma.

III. RESULTS AND DISCUSSION

A. Dense Al plasma created by an XFEL pulse

To demonstrate the physical significance of transient IPD effects for a nonequilibrium plasma, we perform simulations for the situation considered in a recent experiment on XFEL-driven solid-density aluminum [12,33]. In this experiment, a
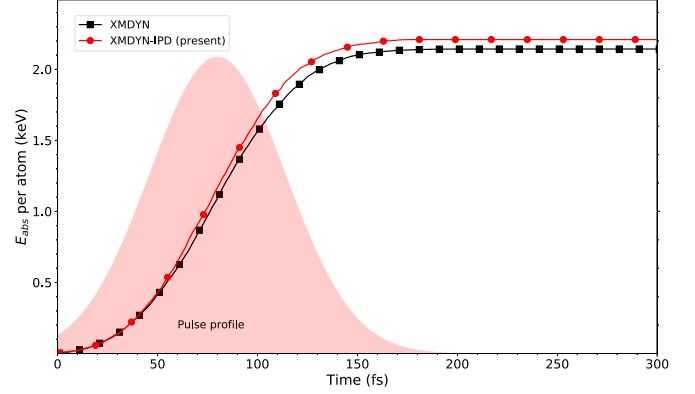

FIG. 2. Time evolution of the absorbed energy per atom in XM-DYN simulations using atomic structures without the IPD effects (XMDYN, black with squares) and with the IPD effects (XMDYN-IPD, red with circles).

solid aluminum target was irradiated using an intense XFEL pulse with a duration of 80 fs full width at half-maximum (FWHM). The pulse contained $\sim 10^{12}$ photons, and the focal size was $9.1 \pm 0.8 \, \mu\text{m}^2$.

The simulated bulk solid-density aluminum target ($n_i = 2.7 \, \text{g/cm}^3 = 0.060\,26 \, \text{Å}^{-3}$) is represented by a supercell that consists of 500 atoms (with a lattice constant of 20.23 Å, containing $5 \times 5 \times 5$ fcc unit cells), starting from the same crystalline geometry where all atoms are initially at rest. We compute five MC-MD realizations (i.e., 2500 different realizations for the atomic ions), which we numerically verified to be sufficient to describe the stochastic x-ray interactions. The x-ray beam parameters used in our calculations follow the experimental conditions. The photon energy is fixed at 1850 eV. The fluence is fixed at $1.0 \times 10^{11} \, \text{ph}/\mu\text{m}^2$ and the spatial fluence distribution of the XFEL pulse is considered uniform for simplicity, assuming that all atoms experience the same fluence throughout the supercell. The temporal pulse shape is chosen as a Gaussian function of 80 fs FWHM, and its peak is centered at 80 fs as shown in Fig. 2. The simulation is performed up to $t = 300$ fs.

The computational time was 11 days (XMDYN) and 47 days (XMDYN-IPD) for each MC-MD realization on an Intel Xenon E5-1650v4 3.60GHz CPU (single core).

B. Time evolution of the charge and deposited energy

First, we compare the energy deposition by photoabsorption between the two different implementations. Figure 2 shows the absorbed energy (equal to the number of absorbed photons times the photon energy) per atom during the XFEL pulse, whose shape is plotted as the colored shade. The black curve is for the original XMDYN implementation using isolated-atomic data, while the red curve is for the present XMDYN-IPD implementation. Overall, the two energy absorption curves are very similar to each other, because photoabsorption at 1850 eV is dominated by K-shell ionization, and its cross section is not much influenced by the IPD effects ($\Delta E \simeq 50-140$ eV; see Fig. 8 in Ref. [61]). For example, the photoionization cross section of Ar^{5+} ($1s^2 2s^2 2p^4$) at 1850 eV is 0.124 Mb, no matter whether IPD is taken into
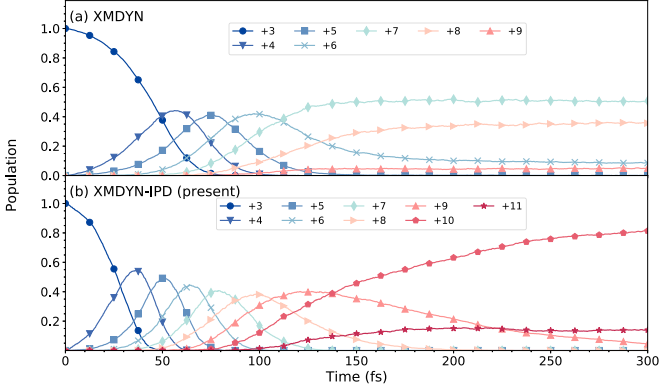
FIG. 3. Time evolution of the charge-state populations simulated using (a) the original XMDYN implementation and (b) the present XMDYN-IPD implementation.
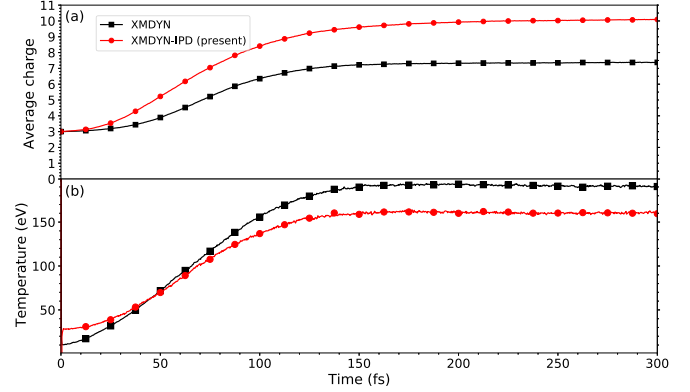

FIG. 4. Time evolution of (a) the average charge and (b) electron temperature in simulations using XMDYN (black with squares) and XMDYN-IPD (red with circles).

account ($\mathrm{IP}_{1s}^{\mathrm{pla}} = 1577$ eV) or not ($\mathrm{IP}_{1s}^{\mathrm{iso}} = 1681$ eV). On the other hand, note also that the absorbed energy with XMDYN-IPD is slightly higher than that with XMDYN ($\sim$40 eV at $t = 300$ fs). Without the IPD effects, K-shell photoionization at 1850 eV is forbidden for $Q > +7$ and double K-shell-hole formation is also energetically blocked for $Q > +6$. With the IPD effects, however, it is allowed to ionize one K-shell electron for $Q \leqslant +10$ and two K-shell electrons for $Q \leqslant +8$. The small increment of the absorbed energy in XMDYN-IPD at the end of time propagation is attributed to these new K-shell photoionization channels that are allowed due to the lowered K-shell IP.

Next, we examine the time evolution of charge-state populations by using the simulation of (a) the original XMDYN and (b) the present XMDYN-IPD, as shown in Fig. 3. To define the atomic charge state, we employ the following definition considering bound states only up to the $2p$ subshell:

$$Q_A = Z_A - \sum_{j}^{1s,2s,2p} n_j^A, \qquad (6)$$

where Z_A is the atomic number and n_j^A is the occupation number for the jth orbital of the atomic ion A. Note that Q_A is different from q_A used in Eq. (1), where q_A is defined with the bound electrons below V_0, mainly because of a subtlety of how M-shell electrons are treated. In the present XMDYN-IPD, the M-shell energy levels are quickly above V_0 and the M-shell electrons are emptied at early times when they see an emerging plasma environment, and $Q_A = q_A$ if there are no quantum electrons in the M shell. As time goes by and high charge states are gradually formed, the M-shell levels drop below V_0 [31,50] and they can be partially and transiently occupied due to the recombination process, as illustrated in Fig. 9 in Appendix B.

Figure 3 clearly shows that high charge states in (b) XMDYN-IPD are populated earlier than in (a) XMDYN. For example, at $t = 50$ fs, Al^{3+} and Al^{4+} are dominant species in (a), whereas in (b) Al^{5+} is predominantly populated. At the end of the pulse, higher charge states are formed in (b) than in (a); for example, Al^{10+} and Al^{11+} are observed in (b), which are absent in (a). Also note that the population

dynamics of XMDYN-IPD do not look fully equilibrated at $t = 300$ fs. The trend of higher charge-state formation in the present XMDYN-IPD as shown in Fig. 3(b) can be understood by the fact that the lowered IP makes higher charge states more accessible, in spite of almost the same amount of deposited energy. Note that the small increment ($\sim$40 eV) in the deposited energy of XMDYN-IPD shown in Fig. 2 may not energetically cause further ionization from Al^{9+} (the maximum charge observed in XMDYN), because the energy required to ionize from Al^{9+} to Al^{10+} is $\sim$195 eV (IPD has been considered), which is larger than the increased amount of energy. It implies that this trend of high charge-state formation may not be associated with the IPD effects in photoabsorption, which solely accounts for the deposited energy, but it probably involves the IPD effects in other processes. This point will be further discussed in Sec. III C.

Figure 4 shows the time evolution of the average charge and electron temperature retrieved from our simulations. The black curve indicates the original XMDYN result, while the red curve refers to the present XMDYN-IPD result. The electron temperature for each simulation snapshot is obtained by fitting the kinetic energy distribution of classical electrons to the Maxwell-Boltzmann distribution function [61,72]. As already illustrated in Fig. 3, the implication of high charge-state formation is quite dramatic in the time evolution of the average charge. The average charge of XMDYN-IPD rapidly deviates from the original XMDYN result, and their difference reaches a value of about $+2.7$ at the end of the simulation. Again, the rise of the average charge in XMDYN-IPD can be explained by lowered IP values, which facilitate more ionization processes. As demonstrated in Fig. 2, the absorbed energy is similar for XMDYN and XMDYN-IPD; however, the higher the average charge is, the more electrons are unbound. As a consequence, in XMDYN-IPD more electrons share the same amount of energy, resulting in an electron temperature in XMDYN-IPD that is lower by $\sim$30 eV than that in XMDYN at the end of simulation. It is also interesting to notice that at the early stage ($t < 50$ fs), the electron temperature in XMDYN-IPD is even higher than in XMDYN, which can be attributed to pressure ionization of most M-shell electrons in XMDYN-IPD at early times.
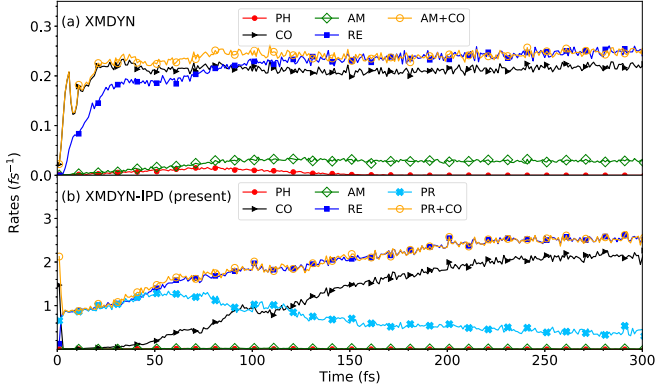
FIG. 5. Rates of atomic processes in simulations using (a) XM-DYN and (b) XMDYN-IPD.

FIG. 6. Rates of core-shell-related atomic processes in simulations using (a) XMDYN and (b) XMDYN-IPD.

C. Analysis of physical processes

To understand how higher charge states are generated in spite of a similar amount of photoabsorption in the XMDYN-IPD implementation, we compare the detailed atomic processes in the two simulation approaches. Figure 5 shows the rates of all processes, including recombination (RE, blue with squares), collisional ionization (CO, black with triangles), photoionization (PH, red with circles), and Auger-Meitner decay (AM, green with diamonds) calculated using (a) XMDYN and (b) XMDYN-IPD. In addition, the newly introduced pressure ionization process (PR, light blue with crosses) is shown in the XMDYN-IPD case. In Fig. 5(a), the collisional ionization process is the major ionizing process, which is supposed to be balanced with the recombination process when the charge-state distribution is equilibrated. Note that no detailed balancing based on equilibrium conditions is enforced in either XMDYN or XMDYN-IPD, thus making them suitable for investigating nonequilibrium dynamics. After the XFEL pulse diminishes ($\gtrsim 160$ fs), the rates of collisional ionization and recombination clearly do not match; instead, the sum of Auger-Meitner decay and collisional ionization rates (AM + CO, orange with open circles) is balanced by the recombination rate. This is because of an *ad hoc* treatment of M-shell electrons in the original XMDYN implementation, where the atomic structure is calculated for an isolated Al atom, and the occupation numbers in the $1s$, $2s$, $2p$, $3s$, and $3p$ subshells are always counted as bound electrons (see the occupation of the M shells in Fig. 9 in Appendix B). When the $3p$ subshell becomes populated via recombination, it may be reionized via either Auger-Meitner decay or collisional ionization. This explains the nonzero AM rate and balancing between RE and AM + CO at the end of the simulation in Fig. 5(a).

In the present XMDYN-IPD implementation, the M shell is treated as bound or unbound depending on whether its energy level is below or above the potential tail V_0. When a negative plasma potential tail emerges at the beginning, the M-shell energy levels of Al are located above V_0. In this case, if recombination happens to the $3p$ subshell, these recombined electrons are immediately ionized via pressure ionization. As high charge states are formed, the M shells are turned into bound states [31,50]. In this case, the $3p$ electrons after recom-
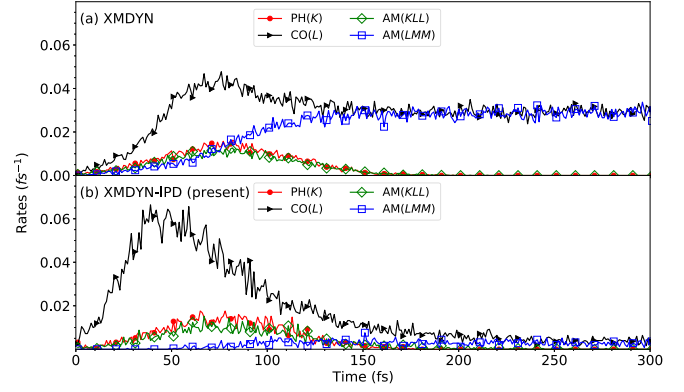
bination are ionized mainly via collisional ionization. Thus, one can see in Fig. 5(b) that the sum of pressure ionization and collisional ionization rates (PR + CO, orange with open circles) is balanced by the recombination rate. At early times, PR is dominantly balanced with RE, while the CO contribution increases as time goes by, indicating that in increasingly more atomic ions the M shell becomes bound (see the occupation of the M shell in Fig. 9 in Appendix B). It is worthwhile to note that the balancing rates (RE and PR + CO) in Fig. 5(b) are an order of magnitude higher than those (RE and AM + CO) in Fig. 5(a), which may be attributed to enhanced collisional ionization due to the IPD effects. The more frequent processes explain why XMDYN-IPD is about four times slower than the original XMDYN in terms of CPU time. Also note that the contribution of photoionization (mainly K-shell electrons) is negligible in comparison with collisional ionization for both Figs. 5(a) and 5(b).

It is known that the IPD values are similar for individual subshells [50], but the impact of IPD depends on individual subshells and respective ionization processes. We have demonstrated that collisional ionization is more responsible than photoionization for plasma formation dynamics (Fig. 5) and that the XMDYN-IPD provides much higher charge states than the original XMDYN [Figs. 3 and 4(a)]. Then, one may ask which subshell in collisional ionization is more responsible for high charge-state formation, particularly the rise of the average charge in the XMDYN-IPD implementation shown in Fig. 4(a). To this end, we examine in Fig. 6 individual subshell contributions to atomic processes. We separate out photoionization, Auger-Meitner decay, and collisional ionization for the different subshells involved: PH(K, L, and M), AM(KLL, KLM, KMM, and LMM), and CO(K, L, and M). Since the atomic charge in Eq. (6) is defined using only K- and L-shell electrons, we plot the rates of atomic processes relevant to the change of occupation numbers in K and L shells in Fig. 6. Note that contributions of PH(L), CO(K), and AM(KMM) are negligible in comparison with others, and AM(KLM) does not change the atomic charge, so they are not plotted. Among the relevant atomic processes, PH(K), AM(KLL), and CO(L) provide $\Delta Q_A = +1$, while only AM(LMM) makes $\Delta Q_A = -1$. In fact, the temporal integral of the sum of rates for these processes, i.e., $R^{\mathrm{PH}(K)}(t) + R^{\mathrm{AM}(KLL)}(t) + R^{\mathrm{CO}(L)}(t) - R^{\mathrm{AM}(LMM)}(t)$, where $R(t)$ is the time-dependent rate, corre-
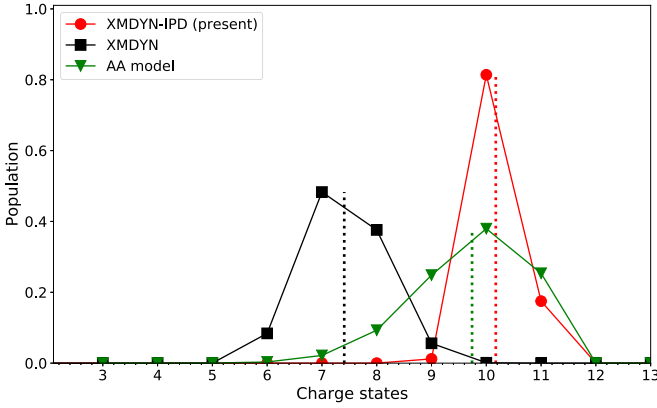
FIG. 7. Charge-state distribution at the end of the simulation using the present XMDYN-IPD (red with circles) and original XM-DYN (black with squares) implementations, in comparison with the AA model at a temperature of 160 eV (green with triangles). The corresponding average charge states are indicated by the vertical dashed lines.

sponds to the average Q_A at the end of simulation. For both (a) XMDYN and (b) XMDYN-IPD, CO(L) is the most dominant channel to create high charge states. In Fig. 6(a) with the original XMDYN implementation, CO(L) is balanced with AM(LMM) at the end of simulation, which is consistent with the previous observation in Fig. 5(a). In Fig. 6(b) with the present XMDYN-IPD implementation, CO(L) becomes more accessible due to lowered L-shell IP, and the area of CO(L) enclosed by the balanced curve of AM(LMM) is larger than that in (a), which is the main reason for the rise of the average charge in XMDYN-IPD shown in Fig. 4(a). For comparison, the CO rates for different subshells and charges calculated with and without the IPD effects are listed in Table I in Appendix C.

D. Comparison with the average-atom model

We have demonstrated in Fig. 3 that our two MC-MD simulation approaches using the atomic structure with and without the IPD effects produce different charge-state distributions (CSDs). The validity of the simulations can be tested by comparing the final equilibrium state with a full quantum-mechanical calculation based on the average-atom (AA) model [50], where thermal equilibrium is assumed and a finite-temperature HFS calculation is performed taking into account the plasma environmental effects. In the AA calculation, both bound and free electrons are treated quantum mechanically by employing a grand-canonical ensemble [50], and the calculated IP values (and thus the IPD effects) are in good agreement [16] with available experimental data [12,33]. Note that the MC-MD simulations describe all dynamical processes until the system reaches equilibrium, whereas the AA model is independent of the history of reaching the equilibrium state.

The CSDs for the equilibrium state in the two MC-MD simulation approaches and for the AA model are shown in Fig. 7. To assure that the CSDs using XMDYN and XMDYN-IPD are equilibrated, the simulated plasmas are further propagated until $t = 400$ fs. The AA model is cal-

culated with an electron temperature of $T_e = 160$ eV, which corresponds to the fitted temperature for the XMDYN-IPD simulation [Fig. 4(b)], and the same atomic density as used in the MC-MD simulations. To calculate the atomic charge state in the AA model, we use the same definition as in Eq. (6), instead of counting electrons with energy levels below the potential tail in the original paper [50]. As shown in Fig. 7, the CSD of the original XMDYN implementation (black) is shifted towards lower charges in comparison with the AA model (green), which exhibits the same trend as observed in the diluted diamond case [72], but the shift is much pronounced in the present solid-density Al case. The CSD simulated with XMDYN-IPD (red) shows a significant improvement with respect to the AA model. The average charge states, indicated by the corresponding vertical dashed lines, show good agreement between XMDYN-IPD and AA, whereas the population profile in the AA model is broader than the present XMDYN-IPD result.

This discrepancy in the width of the CSD can be attributed to differences in the electronic-structure descriptions employed in XMDYN-IPD and AA, respectively. In XMDYN-IPD, orbitals and associated orbital energies are optimized in the presence of the plasma environment for each charge state separately. In the AA model, however, the self-consistent-field procedure determines a universal set of orbitals that must describe all electronic configurations present in the grand-canonical ensemble at a given temperature and atomic density. For instance, within the AA model, the $2p$ binding energy of Al^{q+} is the same for all q. To compute the IPD for each charge state within the AA model, one must choose the temperature that maximizes the population of each charge state. As a consequence, in the AA calculation at a fixed temperature, the ionization potentials of the lower and higher charged ions (other than the dominantly populated one) will be overestimated and underestimated, respectively, which tends to broaden the population profile.

IV. CONCLUSION

In this study, we have demonstrated the role of the plasma environmental effects at the level of atomic structures in MC-MD simulations of dense plasmas. The transient IPD effects are calculated within an NLTE approach. In the present scheme, the external plasma potential and transient IPD values are calculated based on snapshots of the classical particles, and they are incorporated into the computation of atomic structure and atomic data as a resource for the MC-MD simulations. The resulting nonzero potential tail in the atomic-structure calculation provides a consistent way of treating ionization processes. It affects all dynamical ionization processes, including photoionization, Auger-Meitner decay, and collisional ionization, and it mimics pressure ionization due to a dense environment. We have implemented such plasma environmental effects into our MC-MD simulation tool, XMDYN.

To systematically investigate how the plasma environmental effects influence plasma formation dynamics induced by intense XFEL pulses, we have performed simulations of solid-density Al plasmas using two different implementations: XMDYN-IPD with IPD feedback, and the original XMDYN

TABLE I. Collisional ionization rates (in a.u.) calculated from the BEB model for different charge states in plasmas simulated using the atomic structure with and without the IPD effects.

	2s		2p		3s		3p	
Q	w/o IPD	w/ IPD	w/o IPD	w/ IPD	w/o IPD	w/ IPD	w/o IPD	w/ IPD
3	8.3×10^{-5}	2.3×10^{-2}	1.8×10^{-3}	5.4×10^{-1}	8.6×10^{-2}		1.7×10^{-1}	
4	1.2×10^{-2}	3.1×10^{-2}	6.6×10^{-2}	3.1×10^{-1}	4.2×10^{-1}		6.0×10^{-1}	
5	1.9×10^{-2}	5.1×10^{-2}	6.9×10^{-2}	2.9×10^{-1}	3.9×10^{-1}		5.1×10^{-1}	
6	2.3×10^{-2}	6.0×10^{-2}	5.3×10^{-2}	2.0×10^{-1}	3.3×10^{-1}	1.1×10^{3}	4.1×10^{-1}	
7	2.6×10^{-2}	6.8×10^{-2}	3.7×10^{-2}	1.2×10^{-1}	3.0×10^{-1}	4.2×10^{2}	3.5×10^{-1}	
8	1.6×10^{-2}	7.5×10^{-2}	1.1×10^{-2}	6.0×10^{-2}	1.9×10^{-1}	1.6×10^{2}	2.2×10^{-1}	
9	9.8×10^{-3}	7.1×10^{-2}	6.5×10^{-3}	5.5×10^{-2}	1.3×10^{-1}	6.2×10^{1}	1.4×10^{-1}	
10	3.1×10^{-3}	2.4×10^{-2}	3.9×10^{-3}	3.4×10^{-2}	8.9×10^{-2}	6.6×10^{0}	9.6×10^{-2}	1.0×10^{1}

without IPD feedback. Between the two simulation approaches, there is almost no difference in the deposited energy by x-ray absorption. However, the plasma screening effects in the atomic-structure calculation drive the formation of high charge states, resulting in an enhancement of the average charge and a reduction of the electron temperature during the time propagation of XMDYN-IPD simulations. We attribute the dramatic effects observed to the impact of IPD effects on L-shell collisional ionization, rather than inner-shell photoionization. Our present implementation of XMDYN with IPD feedback is free from thermal equilibrium requirements. To test its validity, we have presented the charge-state distribution calculated using XMDYN-IPD after thermalization, in comparison with a full quantum-mechanical average-atom calculation based on thermal equilibrium.

Our results suggest that a proper treatment of the IPD and plasma environmental effects is critical for accurate simulations of the formation and thermalization dynamics of dense plasmas. We anticipate that our present approach based on NLTE will provide important insights into the ultrafast nonequilibrium dynamics of warm and hot dense plasmas in extreme conditions, e.g., induced by gigawatt- or terawatt-attosecond x-ray pulses [76,77], where electron thermalization on the timescale of the pulse duration cannot be guaranteed.
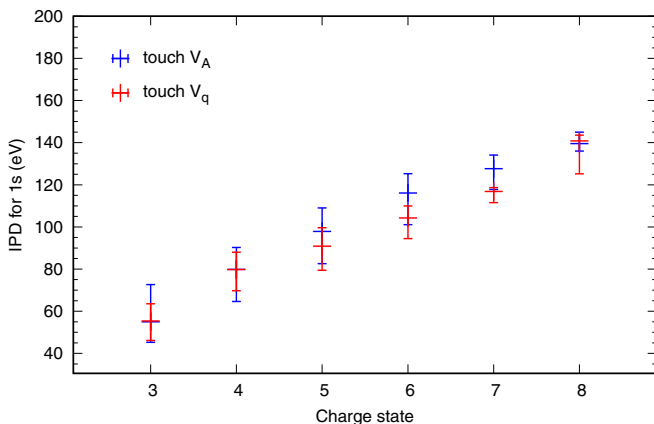
APPENDIX A: IMPLEMENTATION OF THE TOUCHING POTENTIAL ALGORITHM

Figure 8 shows calculated IPDs using two different choices for the approximated potential used in the touching potential algorithm:

$$\text{touch } V_A: V_A^{\text{approx}}(r) = -\frac{q_A + 1}{r} + V_A^{\text{env}}(r),$$

$$\text{touch } V_q: V_A^{\text{approx}}(r) = -\frac{q_A + 1}{r} + V_{q=q_A}^{\text{env}}(r).$$

In the present work, we employed V_q to maintain consistency with the environmental potential used in Eq. (1).

APPENDIX B: TIME EVOLUTION OF *M*-SHELL OCCUPATION NUMBERS

Figure 9 shows M-shell occupation numbers as a function of time in XMDYN and XMDYN-IPD. Note that the M shell is always considered bound in XMDYN, but not in XMDYN-IPD. In the latter, whether a level corresponds to a bound state depends on whether the energy level is below or above the potential tail during the time propagation.
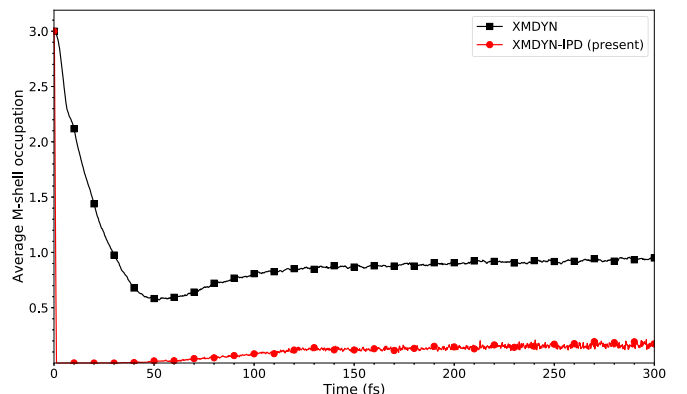

FIG. 8. Comparison of the ionization potential depression for two different implementations of the approximated potential.

FIG. 9. Time evolution of the average *M*-shell occupation numbers in XMDYN and XMDYN-IPD.

APPENDIX C: COLLISIONAL IONIZATION RATES

The collisional ionization rate for the (n, l)-subshell for the charge q is obtained using

$$R_{q,nl} = \int_0^\infty v \rho_e(v) \sigma_{q,nl}(v) dv,$$

where v is the velocity, $\rho_e(v)$ is the velocity distribution of the electrons at a time when the given charge state is dominant, and $\sigma_{q,nl}(v)$ is the collisional ionization cross section calculated from the binary-encounter-Bethe (BEB) model [78]. The collisional ionization rates for simulations using the atomic structure with and without the IPD effects are listed in Table I. The calculated rates are enhanced in the presence of the IPD effects.

[1] R. P. Drake, *High-Energy-Density Physics: Fundamentals, Inertial Fusion, and Experimental Astrophysics*, 1st ed. (Springer-Verlag, Berlin, 2006), Chap. 1, pp. 5–8.

[2] R. J. Taylor, *The Stars: Their Structure and Evolution*, 2nd ed. (Cambridge University Press, Cambridge, England, 1994).

[3] F. J. Rogers and C. A. Iglesias, Astrophysical opacity, Science **263**, 50 (1994).

[4] G. Chabrier, Plasma physics and planetary astrophysics, Plasma Phys. Control. Fusion **51**, 124014 (2009).

[5] R. Helled, J. D. Anderson, M. Podolak, and G. Schubert, Interior models of Uranus and Neptune, Astrophys. J. **726**, 15 (2011).

[6] T. Guillot, Interiors of giant planets inside and outside the solar system, Science **286**, 72 (1999).

[7] B. Militzer, F. Soubiran, S. M. Wahl, and W. Hubbard, Understanding Jupiter's interior, J. Geophys. Res. Planets **121**, 1552 (2016).

[8] J. Lindl, Development of the indirect-drive approach to inertial confinement fusion and the target physics basis for ignition and gain, Phys. Plasmas **2**, 3933 (1995).

[9] S. H. Glenzer, B. J. MacGowan, P. Michel, N. B. Meezan, L. J. Suter, S. N. Dixit, J. L. Kline, G. A. Kyrala, D. K. Bradley, D. A. Callahan, E. L. Dewald, L. Divol, E. Dzenitis, M. J. Edwards, A. V. Hamza, C. A. Haynam, D. E. Hinkel, D. H. Kalantar, J. D. Kilkenny, O. L. Landen *et al.*, Symmetric inertial confinement fusion implosions at ultra-high laser energies, Science **327**, 1228 (2010).

[10] E. A. Seddon, J. A. Clarke, D. J. Dunning, C. Masciovecchio, C. J. Milne, F. Parmigiani, D. Rugg, J. C. H. Spence, N. R. Thompson, K. Ueda, S. M. Vinko, J. S. Wark, and W. Wurth, Short-wavelength free-electron laser sources and science: A review, Rep. Prog. Phys. **80**, 115901 (2017).

[11] S. H. Glenzer, L. B. Fletcher, E. Galtier, B. Nagler, R. Alonso-Mori, B. Barbrel, S. B. Brown, D. A. Chapman, Z. Chen, C. B. Curry, F. Fiuza, E. Gamboa, M. Gauthier, D. O. Gericke, A. Gleason, S. Goede, E. Granados, P. Heimann, J. Kim, D. Kraus *et al.*, Matter under extreme conditions experiments at the linac coherent light source, J. Phys. B **49**, 092001 (2016).

[12] S. M. Vinko, O. Ciricosta, B. I. Cho, K. Engelhorn, H.-K. Chung, C. R. D. Brown, T. Burian, J. Chalupský, R. W. Falcone, C. Graves, V. Hájková, A. Higginbotham, L. Juha, J. Krzywinski, H. J. Lee, M. Messerschmidt, C. D. Murphy, Y. Ping, A. Scherz, W. Schlotter *et al.*, Creation and diagnosis of a solid-density plasma with an x-ray free-electron laser, Nature (London) **482**, 59 (2012).

[13] J. Bauche, C. Bauche-Arnoult, and O. Peyrusse, *Atomic Properties in Hot Plasmas*, 1st ed. (Springer International, Cham, Switzerland, 2015).

[14] D. Agassi, Phenomenological model for pisosecond-pulse laser annealing of semiconductors, J. Appl. Phys. **55**, 4376 (1984).

[15] P. L. Silvestrelli, A. Alavi, M. Parrinello, and D. Frenkel, *Ab initio* Molecular Dynamics Simulation of Laser Melting of Silicon, Phys. Rev. Lett. **77**, 3149 (1996).

[16] J. J. Bekx, S.-K. Son, B. Ziaja, and R. Santra, Electronic-structure calculations for nonisothermal warm dense matter, Phys. Rev. Research **2**, 033061 (2020).

[17] S. I. Anisimov, B. L. Kapeliovich, and T. L. Perel'man, Electron emission from metal surfaces exposed to ultrashort laser pulses, Sov. Phys. JETP **39**, 375 (1974).

[18] B. Rethfeld, D. S. Ivanov, M. E. Garcia, and S. I. Anisimov, Modelling ultrafast laser ablation, J. Phys. D **50**, 193001 (2017).

[19] H. A. Scott, Cretin—a radiative transfer capability for laboratory plasmas, J. Quant. Spectrosc. Radiat. Transf. **71**, 689 (2001).

[20] H.-K. Chung, M. Chen, W. Morgan, Y. Ralchenko, and R. Lee, Flychk: Generalized population kinetics and spectral model for rapid spectroscopic analysis for all elements, High Energy Density Phys. **1**, 3 (2005).

[21] H.-K. Chung and R. W. Lee, Applications of NLTE population kinetics, High Energy Density Phys. **5**, 1 (2009).

[22] S. Hansen, H.-K. Chung, C. Fontes, Y. Ralchenko, H. Scott, and E. Stambulchik, Review of the 10th Non-LTE code comparison workshop, High Energy Density Phys. **35**, 100693 (2020).

[23] X. Han, L. Li, Z. Dai, and W. Zheng, MAICRM: A general model for rapid simulation of hot dense plasma spectra, High Energy Density Phys. **39**, 100943 (2021).

[24] B. Deschaud, O. Peyrusse, and F. B. Rosmej, Simulation of XFEL induced fluorescence spectra of hollow ions and studies of dense plasma effects, Phys. Plasmas **27**, 063303 (2020).

[25] D. R. Bates, A. E. Kingston, and R. W. P. McWhirter, Recombination between electrons and atomic ions, I. optically thin plasmas, Proc. R. Soc. London A **267**, 297 (1962).

[26] *Modern Methods in Collisional-Radiative Modeling of Plasmas*, 1st ed., edited by Y. Ralchenko (Springer, Cham, Switzerland, 2016).

[27] B. F. Murphy, T. Osipov, Z. Jurek, L. Fang, S.-K. Son, M. Mucke, J. H. D. Eland, V. Zhaunerchyk, R. Feifel, L. Avaldi, P. Bolognesi, C. Bostedt, J. D. Bozek, J. Grilj, M. Guehr, L. J. Frasinski, J. Glownia, D. T. Ha, K. Hoffmann, E. Kukk *et al.*, Femtosecond x-ray-induced explosion of C_{60} at extreme intensity, Nat. Commun. **5**, 4281 (2014).

[28] Z. Jurek, S.-K. Son, B. Ziaja, and R. Santra, *XMDYN* and *XATOM*: Versatile simulation tools for quantitative modeling of X-ray free-electron laser induced dynamics of matter, J. Appl. Crystallogr. **49**, 1048 (2016).

[29] J. C. Stewart and K. D. Pyatt, Jr., Lowering of ionization potentials in plasmas, Astrophys. J. **144**, 1203 (1966).

[30] G. Ecker and W. Kröll, Lowering of the ionization energy for a plasma in thermodynamic equilibrium, Phys. Fluids **6**, 62 (1963).

[31] D. J. Hoarty, P. Allan, S. F. James, C. R. D. Brown, L. M. R. Hobbs, M. P. Hill, J. W. O. Harris, J. Morton, M. G. Brookes, R. Shepherd, J. Dunn, H. Chen, E. Von Marley, P. Beiersdorfer, H. K. Chung, R. W. Lee, G. Brown, and J. Emig, Observations of the Effect of Ionization-Potential Depression in Hot Dense Plasma, Phys. Rev. Lett. **110**, 265003 (2013).

[32] D. Hoarty, P. Allan, S. James, C. Brown, L. Hobbs, M. Hill, J. Harris, J. Morton, M. Brookes, R. Shepherd, J. Dunn, H. Chen, E. V. Marley, P. Beiersdorfer, H. Chung, R. Lee, G. Brown, and J. Emig, The first data from the Orion laser; measurements of the spectrum of hot, dense aluminium, High Energy Density Phys. **9**, 661 (2013).

[33] O. Ciricosta, S. M. Vinko, H.-K. Chung, B.-I. Cho, C. R. D. Brown, T. Burian, J. Chalupský, K. Engelhorn, R. W. Falcone, C. Graves, V. Hájková, A. Higginbotham, L. Juha, J. Krzywinski, H. J. Lee, M. Messerschmidt, C. D. Murphy, Y. Ping, D. S. Rackstraw, A. Scherz *et al.*, Direct Measurements of the Ionization Potential Depression in a Dense Plasma, Phys. Rev. Lett. **109**, 065002 (2012).

[34] B. Ziaja, Z. Jurek, N. Medvedev, S.-K. Son, R. Thiele, and S. Toleikis, Photoelectron spectroscopy method to reveal ionization potential lowering in nanoplasmas, J. Phys. B **46**, 164009 (2013).

[35] T. R. Preston, S. M. Vinko, O. Ciricosta, H.-K. Chung, R. W. Lee, and J. S. Wark, The effects of ionization potential depression on the spectra emitted by hot dense aluminium plasmas, High Energy Density Phys. **9**, 258 (2013).

[36] L. B. Fletcher, A. L. Kritcher, A. Pak, T. Ma, T. Döppner, C. Fortmann, L. Divol, O. S. Jones, O. L. Landen, H. A. Scott, J. Vorberger, D. A. Chapman, D. O. Gericke, B. A. Mattern, G. T. Seidler, G. Gregori, R. W. Falcone, and S. H. Glenzer, Observations of Continuum Depression in Warm Dense Matter with X-Ray Thomson Scattering, Phys. Rev. Lett. **112**, 145004 (2014).

[37] O. Ciricosta, S. M. Vinko, B. Barbrel, D. S. Rackstraw, T. R. Preston, T. Burian, J. Chalupský, B. I. Cho, H. K. Chung, G. L. Dakovski, K. Engelhorn, V. Hájková, P. Heimann, M. Holmes, L. Juha, J. Krzywinski, R. W. Lee, S. Toleikis, J. J. Turner, U. Zastrau *et al.*, Measurements of continuum lowering in solid-density plasmas created from elements and compounds, Nat. Commun. **7**, 11713 (2016).

[38] D. Kraus, B. Bachmann, B. Barbrel, R. W. Falcone, L. B. Fletcher, S. Frydrych, E. J. Gamboa, M. Gauthier, D. O. Gericke, S. H. Glenzer, S. Göde, E. Granados, N. J. Hartley, J. Helfrich, H. J. Lee, B. Nagler, A. Ravasio, W. Schumaker, J. Vorberger, and T. Döppner, Characterizing the ionization potential depression in dense carbon plasmas with high-precision spectrally resolved x-ray scattering, Plasma Phys. Control. Fusion **61**, 014015 (2019).

[39] M. F. Kasim, J. S. Wark, and S. M. Vinko, Validating continuum lowering models via multi-wavelength measurements of integrated x-ray emission, Sci. Rep. **8**, 6276 (2018).

[40] B. Crowley, Continuum lowering—A new perspective, High Energy Density Phys. **13**, 84 (2014).

[41] C. A. Iglesias, A plea for a reexamination of ionization potential depression measurements, High Energy Density Phys. **12**, 5 (2014).

[42] A. Calisti, S. Ferri, and B. Talin, Ionization potential depression for non equilibrated aluminum plasmas, J. Phys. B **48**, 224003 (2015).

[43] A. Calisti, S. Ferri, and B. Talin, Ionization potential depression in hot dense plasmas through a pure classical model, Contrib. Plasma Phys. **55**, 360 (2015).

[44] M. Stransky, Monte Carlo simulations of ionization potential depression in dense plasmas, Phys. Plasmas **23**, 012708 (2016).

[45] C. Lin, G. Röpke, W.-D. Kraeft, and H. Reinholz, Ionization-potential depression and dynamical structure factor in dense plasmas, Phys. Rev. E **96**, 013202 (2017).

[46] G. Röpke, D. Blaschke, T. Döppner, C. Lin, W.-D. Kraeft, R. Redmer, and H. Reinholz, Ionization potential depression and Pauli blocking in degenerate plasmas at extreme densities, Phys. Rev. E **99**, 033201 (2019).

[47] F. B. Rosmej, Ionization potential depression in an atomic-solid-plasma picture, J. Phys. B **51**, 09LT01 (2018).

[48] J.-C. Pain, On the Li-Rosmej analytical formula for energy level shifts in dense plasmas, High Energy Density Phys. **31**, 99 (2019).

[49] X. Li, F. B. Rosmej, V. S. Lisitsa, and V. A. Astapenko, An analytical plasma screening potential based on the self-consistent-field ion-sphere model, Phys. Plasmas **26**, 033301 (2019).

[50] S.-K. Son, R. Thiele, Z. Jurek, B. Ziaja, and R. Santra, Quantum-Mechanical Calculation of Ionization-Potential Lowering in Dense Plasmas, Phys. Rev. X **4**, 031004 (2014).

[51] S. M. Vinko, O. Ciricosta, and J. S. Wark, Density functional theory calculations of continuum lowering in strongly coupled plasmas, Nat. Commun. **5**, 3533 (2014).

[52] J. Zeng, Y. Li, C. Gao, and J. Yuan, Screening potential and continuum lowering in a dense plasma under solar-interior conditions, Astron. Astrophys. **634**, A117 (2020).

[53] K. P. Driver, F. Soubiran, and B. Militzer, Path integral monte carlo simulations of warm dense aluminum, Phys. Rev. E **97**, 063207 (2018).

[54] S. X. Hu, Continuum Lowering and Fermi-Surface Rising in Strongly Coupled and Degenerate Plasmas, Phys. Rev. Lett. **119**, 065001 (2017).

[55] S. P. Hau-Riege, Nonequilibrium electron dynamics in materials driven by high-intensity x-ray pulses, Phys. Rev. E **87**, 053102 (2013).

[56] R. R. Fäustlin, T. Bornath, T. Döppner, S. Düsterer, E. Förster, C. Fortmann, S. H. Glenzer, S. Göde, G. Gregori, R. Irsig, T. Laarmann, H. J. Lee, B. Li, K.-H. Meiwes-Broer, J. Mithen, B. Nagler, A. Przystawik, H. Redlin, R. Redmer, H. Reinholz *et al.*, Observation of Ultrafast Nonequilibrium Collective Dynamics in Warm Dense Hydrogen, Phys. Rev. Lett. **104**, 125002 (2010).

[57] K. K. Ostrikov, F. Beg, and A. Ng, Colloquium: Nanoplasmas generated by intense radiation, Rev. Mod. Phys. **88**, 011001 (2016).

[58] N. Medvedev, U. Zastrau, E. Förster, D. O. Gericke, and B. Rethfeld, Short-Time Electron Dynamics in Aluminum Excited by Femtosecond Extreme Ultraviolet Radiation, Phys. Rev. Lett. **107**, 165003 (2011).

[59] M. Makita, I. Vartiainen, I. Mohacsi, C. Caleman, A. Diaz, H. O. Jönsson, P. Juranić, N. Medvedev, A. Meents, A. Mozzanica, N. L. Opara, C. Padeste, V. Panneels, V. Saxena, M. Sikorski, S. Song, L. Vera, P. R. Willmott, P. Beaud, C. J. Milne *et al.*, Femtosecond phase-transition in hard x-ray excited bismuth, Sci. Rep. **9**, 602 (2019).

[60] N. J. Hartley, J. Grenzer, W. Lu, L. G. Huang, Y. Inubushi, N. Kamimura, K. Katagiri, R. Kodama, A. Kon, V. Lipp, M. Makita, T. Matsuoka, N. Medvedev, S. Nakajima, N. Ozaki, T. Pikuz, A. V. Rode, K. Rohatsch, D. Sagae, A. K. Schuster *et al.*, Ultrafast anisotropic disordering in graphite driven by intense hard x-ray pulses, High Energy Density Phys. **32**, 63 (2019).

[61] R. Jin, M. M. Abdullah, Z. Jurek, R. Santra, and S.-K. Son, Transient ionization potential depression in nonthermal dense plasmas at high x-ray intensity, Phys. Rev. E **103**, 023203 (2021).

[62] S.-K. Son, L. Young, and R. Santra, Impact of hollow-atom formation on coherent x-ray scattering at high intensity, Phys. Rev. A **83**, 033402 (2011).

[63] D. Matsakis, A. Coster, B. Laster, and R. Sime, A renaming proposal: "The Auger-Meitner effect," Phys. Today **72**, 10 (2019).

[64] T. Tachibana, Z. Jurek, H. Fukuzawa, K. Motomura, K. Nagaya, S. Wada, P. Johnsson, M. Siano, S. Mondal, Y. Ito, M. Kimura, T. Sakai, K. Matsunami, H. Hayashita, J. Kajikawa, X. J. Liu, E. Robert, C. Miron, R. Feifel, J. P. Marangos *et al.*, Nanoplasma formation by high intensity hard x-rays, Sci. Rep. **5**, 10977 (2015).

[65] Y. Kumagai, Z. Jurek, W. Xu, H. Fukuzawa, K. Motomura, D. Iablonskyi, K. Nagaya, S.-i. Wada, S. Mondal, T. Tachibana, Y. Ito, T. Sakai, K. Matsunami, T. Nishiyama, T. Umemoto, C. Nicolas, C. Miron, T. Togashi, K. Ogawa, S. Owada *et al.*, Radiation-Induced Chemical Dynamics in Ar Clusters Exposed to Strong X-Ray Pulses, Phys. Rev. Lett. **120**, 223201 (2018).

[66] Y. Kumagai, Z. Jurek, W. Xu, H. Fukuzawa, K. Motomura, D. Iablonskyi, K. Nagaya, S.-i. Wada, S. Mondal, T. Tachibana, Y. Ito, T. Sakai, K. Matsunami, T. Nishiyama, T. Umemoto, C. Nicolas, C. Miron, T. Togashi, K. Ogawa, S. Owada *et al.*, Real-time observation of disintegration processes within argon clusters ionized by a hard-x-ray pulse of moderate fluence, Phys. Rev. A **101**, 023412 (2020).

[67] Y. Kumagai, Z. Jurek, W. Xu, V. Saxena, H. Fukuzawa, K. Motomura, D. Iablonskyi, K. Nagaya, S. ichi Wada, Y. Ito, T. Takanashi, S. Yamada, Y. Sakakibara, T. Nishiyama, T. Umemoto, M. Patanen, J. D. Bozek, I. Dancus, M. Cernaianu, C. Miron *et al.*, Suppression of thermal nanoplasma emission in clusters strongly ionized by hard x-rays, J. Phys. B **54**, 044001 (2021).

[68] N. Berrah, A. Sanchez-Gonzalez, Z. Jurek, R. Obaid, H. Xiong, R. J. Squibb, T. Osipov, A. Lutman, L. Fang, T. Barillot, J. D. Bozek, J. Cryan, T. J. A. Wolf, D. Rolles, R. Coffee, K. Schnorr, S. Augustin, H. Fukuzawa, K. Motomura, N. Niebuhr *et al.*, Femtosecond-resolved observation of the fragmentation of buckminsterfullerene following x-ray multiphoton ionization, Nat. Phys. **15**, 1279 (2019).

[69] R. Boll, J. M. Schäfer, B. Richard, K. Fehre, G. Kastirke, Z. Jurek, M. S. Schöffler, M. M. Abdullah, N. Anders, T. M. Baumann, S. Eckart, B. Erk, A. De Fanis, R. Dörner, S. Grundmann, P. Grychtol, A. Hartung, M. Hofmann, M. Ilchen, L. Inhester *et al.*, X-ray multiphoton-induced Coulomb explosion images complex single molecules, Nat. Phys. **18**, 423 (2022).

[70] K. Nass, A. Gorel, M. M. Abdullah, A. V. Martin, M. Kloos, A. Marinelli, A. Aquila, T. R. M. Barends, F.-J. Decker, R. B. Doak, L. Foucar, E. Hartmann, M. Hilpert, M. S. Hunter, Z. Jurek, J. E. Koglin, A. Kozlov, A. A. Lutman, G. N. Kovacs, C. M. Roome *et al.*, Structural dynamics in proteins induced by and probed with x-ray free-electron laser pulses, Nat. Commun. **11**, 1814 (2020).

[71] M. M. Abdullah, Z. Jurek, S.-K. Son, and R. Santra, Calculation of x-ray scattering patterns from nanocrystals at high x-ray intensity, Struct. Dyn. **3**, 054101 (2016).

[72] M. M. Abdullah, Anurag, Z. Jurek, S.-K. Son, and R. Santra, Molecular-dynamics approach for studying the nonequilibrium behavior of x-ray-heated solid-density matter, Phys. Rev. E **96**, 023205 (2017).

[73] M. M. Abdullah, S.-K. Son, Z. Jurek, and R. Santra, Towards the theoretical limitations of X-ray nanocrystallography at high intensity: The validity of the effective-form-factor description, IUCrJ **5**, 699 (2018).

[74] H. L. Skriver, *The LMTO Method: Muffin-Tin Orbitals and Electronic Structure*, 1st ed. (Springer-Verlag, Berlin, 1984).

[75] R. M. More, Pressure ionization, resonances, and the continuity of bound and free states, in *Advances in Atomic and Molecular Physics*, edited by D. R. Bates and B. Bederson (Academic, Orlando, 1985), Vol. 21, pp. 305–356.

[76] E. Prat and S. Reiche, Simple Method to Generate Terawatt-Attosecond X-Ray Free-Electron-Laser Pulses, Phys. Rev. Lett. **114**, 244801 (2015).

[77] J. Duris, S. Li, T. Driver, E. G. Champenois, J. P. MacArthur, A. A. Lutman, Z. Zhang, P. Rosenberger, J. W. Aldrich, R. Coffee, G. Coslovich, F.-J. Decker, J. M. Glownia, G. Hartmann, W. Helml, A. Kamalov, J. Knurr, J. Krzywinski, M.-F. Lin, J. P. Marangos *et al.*, Tunable isolated attosecond x-ray pulses with gigawatt peak power from a free-electron laser, Nat. Photon. **14**, 30 (2020).

[78] Y.-K. Kim and M. E. Rudd, Binary-encounter-dipole model for electron-impact ionization, Phys. Rev. A **50**, 3954 (1994).